EES Batteries

PAPER

View Article Online
View Journal

Cite this: DOI: 10.1039/d6eb00051g

Comparing the safety of graphite and silicon negative active materials in lithium ion batteries

L. Schrief, [a] L. Trojahn,[a] J. Jang,[b] N. Fehlings,[a] S. Nowak, [a] M. Winter[a,c] and M. Börner *[a]

For high-energy lithium ion batteries, silicon is a promising alternative to the state-of-the-art negative electrode active material graphite. Besides the improvement of the electrochemical performance of Si-based electrodes, the thermal stability of these electrodes is crucial for safe battery operation. Therefore, the thermal stabilities of graphitic and Si-based electrodes are compared in this study. Initially, analyses focus on electrodes in combination with electrolyte using differential scanning calorimetry to gain information on onset temperatures and heat release, as well as heat-ramp experiments in an accelerating rate calorimeter (ARC), including pressure and gas analysis. Finally, the thermal behavior is examined at the cell level with both negative active materials in an ARC. It is shown that Si-based negative electrodes cause distinctly stronger exothermic reactions compared to graphite-based electrodes with the same capacity. This increased reactivity and the generation of high amounts of hydrogen accelerate thermal runaway in Si-based cells. Furthermore, this study indicates that the addition of pressure and gas analysis to thermal investigations enables crucial additional conclusions to be drawn on the thermal behavior of negative electrodes. In summary, this study reveals a reduced thermal stability of Si-based electrodes compared to graphite-based electrodes and underlines the relevance of pressure and gas analysis for thermal stability investigations.

Received 3rd March 2026,
Accepted 22nd May 2026

DOI: 10.1039/d6eb00051g

rsc.li/EESBatteries

Broader context

Considering the ever-increasing demand to maximize the performance of electrochemical energy storage systems, state-of-the-art battery technologies need to constantly improve. Consequently, the ongoing search on superior active materials focuses mostly on optimizing energy density, fast charge capability, lifetime, and costs. Besides these factors, safety is considered crucial for future battery systems and, thus, it is necessary to comprehend the safety properties in detail to tailor strategies that enable safe operation. In this context, silicon is one of the most promising negative active materials for future lithium ion batteries due to its nearly ten times higher theoretical specific capacity compared to graphite as a state-of-the-art material. However, apart from their limited cycle life due to enormous volume changes during operation, the safety properties of Si-based electrodes and battery cells are widely unexplored. Therefore, this study presents a comparative thermal analysis of graphitic and Si-based electrodes and battery cells including associated gas evolution as an additional, and equally important, safety-determining factor. It was shown that Si-based negative electrodes cause distinctly stronger exothermic reactions compared to graphite-based electrodes, which was attributed to different degradation mechanisms and evolving reactive gases. Overall, the reported findings can help develop and design safe high-energy silicon-based lithium ion batteries.

Introduction

Lithium ion batteries (LIBs) are energy storage systems that are widely used in various applications, such as portable electric devices, electric vehicles and stationary energy storage systems.[1,2] They exhibit good energy efficiency as well as a low self-discharge.[3] Furthermore, LIBs benefit from great longevity and high energy density compared to other rechargeable battery systems.[4] There are several possibilities to further increase the energy density of LIBs. One of them is the substitution of graphite as a state-of-the-art negative electrode active material by silicon (Si). Due to its distinctly higher specific capacity of 3579 mAh g^{-1} (for $Li_{15}Si_4$) compared to 372 mAh g^{-1} for graphite and a low average lithiation/delithiation potential of ~0.4 V *vs.* $Li|Li^+$ (0.1 V *vs.* $Li|Li^+$ for graphite), Si is considered a promising candidate for the next generation of high-energy LIBs.[5,6] Main challenges for Si-based negative electrodes are caused by the enormous volume changes of Si of up to 280% during lithiation/delithiation.[7] These induce high

[a]MEET Battery Research Center, University of Münster, D-48149 Münster, Germany. E-mail: markus.boerner@uni-muenster.de
[b]LG Energy Solution, R&D Campus Daejeon, 188 Munji-ro, Yuseong-gu, Daejeon 34122, Korea
[c]Helmholtz-Institute Münster, IMD-4, Research Center Jülich GmbH, D-48149 Münster, Germany

mechanical stress, an extensive solid electrolyte interphase (SEI) growth, and concomitant high loss of active lithium. As a consequence, Si-based LIBs suffer from a fast capacity decay and a poor cycle life.[8–11] Thus, several approaches have been developed and reported to tackle these issues regarding battery performance and lifetime. Therein, the utilization of Si nanoparticles to mitigate pulverization effects,[12–14] the modification of the particle structure[15,16] and the addition of a carbon coating to improve cycling stability and rate capability[17] or the variation of the electrolyte composition to create a more stable SEI and therefore suppressing Si particle pulverization[18–20] have been investigated, amongst others. Furthermore, Graf *et al.* showed that the operation of Si-based negative electrodes under capacity-limited conditions enables long-term cycling performance. In this way, the capacity of Si is only partially utilized, but it is still higher than the full capacity use of the state-of-the-art anode material graphite and it prevents particle disintegration by maintaining a crystalline Si phase.[21] Despite the above developments, the commercialization of Si-based LIBs is still at an early stage due to several remaining challenges.[22]

In general, there has been only a minor focus on the safety properties of Si-based negative electrodes and complete cells, although safety considerations become increasingly important with rising energy densities.[23] Sources of abuse of LIBs can be classified into three categories: mechanical, electrical and thermal abuse. These different types do not occur individually, but they typically cause interdependent consecutive processes that lead to heat generation of single cell components or complete cells.[24,25] Therefore, the thermal stability of the individual components is considered the most relevant safety property of LIBs.[26] In most scenarios of abuse, the onset of exothermic reactions occurs at the negative electrode. For graphitic negative electrodes, it is initiated by the thermal breakdown of the SEI at temperatures around 100 °C.[27–32] Thermally metastable (mostly organic) SEI components are decomposed and the electrode surface is partially exposed to the electrolyte. As a consequence, lithium ions are thermally de-intercalated from the graphite electrode, which causes exothermic reactions with the electrolyte.[31] With rising temperature, further exothermic reactions between lithiated graphite and the electrolyte are induced, which are dependent on the state of charge (SOC) and the state of health (SOH, incl. Li plating).[31,32] Moreover, the occurring decomposition reactions depend on the electrolyte composition since the electrolyte is directly involved in these reactions.[33,34]

With rising temperature, layered transition metal oxides, such as lithium nickel manganese cobalt oxide (NMC)[35] or lithium nickel cobalt aluminum oxide (NCA),[36] which are often used as cathode active materials in LIBs, thermally degrade and undergo phase transitions. These phase transitions from the initially layered structure to a spinel-type and finally to a rock-salt structure can already start at temperatures of 135 °C and depend on the elemental composition and the degree of delithiation. Concomitant with this, oxygen is released from the structure leading to highly exothermic reactions with the flammable electrolyte and possibly fire and explosion of the battery cell. In this worst-case scenario, which is called thermal runaway, the heat generation is too high to stop. There is no consistent definition for the thermal runaway of a battery cell, but different definitions with self-heating rates exceeding thresholds from 10 °C min^{-1} up to 60 °C min^{-1} are applied.[37,38] Besides these quantitative metrics, which vary for different cell chemistries,[39] an abrupt increase of the self-heating rate can also be applied as an alternative qualitative definition for thermal runaway.[40] Due to the release of oxygen at elevated temperatures, the positive electrode is generally considered to play a decisive role in contributing to the thermal runaway of LIBs.[41,42]

For Si-based negative electrodes, the characterization of the thermal behavior has not been investigated in detail so far. Profatilova *et al.* observed the thermal decomposition of the SEI on a lithiated negative electrode based on Si nanoparticles between 77 °C and 107 °C.[43] Therein, the conducting salt $LiPF_6$ was assigned an important role in the thermal stabilization of the electrode in combination with a carbonate-based electrolyte at temperatures below 140 °C. Beyond that, the main heat generation occurred between 150 °C and 300 °C due to exothermic decomposition reactions between lithiated Si nanoparticles and the electrolyte. Furthermore, the thermal behavior of Si-based electrodes was reported to strongly depend on the Si particle size. The exact decomposition mechanism of Si-based electrodes remained unclear. Park and Lee demonstrated a shift of exothermic reactions to lower temperatures for smaller particle sizes and mentioned reduced ion transport paths and a larger surface area for smaller Si particles as a possible explanation for this.[44] Simultaneously, the total amount of generated heat exhibited a rising trend with decreasing particle sizes for temperatures up to 300 °C, but a declining trend when heated up to 500 °C. As the thermal behavior is especially relevant for temperatures below 300 °C, it was concluded that the thermal stability of negative electrodes based on nano-sized Si needs to be improved. Wang and Dahn directly compared the thermal stability of Si-based negative electrodes to the thermal stability of graphitic electrodes.[45] It was stated that both active materials containing the same amount of lithium, and thus having the same capacity, showed similar thermal behavior in combination with the same electrolyte. Additionally, a lower reactivity was concluded for lithiated Si samples in comparison with graphitic ones due to the formation of a thicker protective layer of reaction products on the surface of Si-based electrodes. However, the sensitivity of the presented method with varying and comparably small sample amounts for both active materials might complicate the validity and comparability of the obtained results. Overall, a comparative analysis of the thermal decomposition mechanisms for both active materials has not been reported yet.[46] Furthermore, pressure and gas analysis might be necessary, besides thermal considerations, to give further insights into the thermal behavior of Si-based electrodes.

In this study, the thermal stabilities of graphitic and of Si-based negative electrodes containing the same amount of Li, thus at the same absolute capacity, are compared. The study

includes thermal analysis of combinations of charged electrodes with electrolyte by differential scanning calorimetry (DSC) and heat-ramp experiments as well as thermal analysis at the cell level by accelerating rate calorimetry (ARC) in heat–wait–seek (HWS) mode to compare characteristic onset temperatures as well as heat generation among both active materials. To gather additional information to the thermal data and to get further insights into the thermal behavior of the active materials, the pressure was monitored during heat-ramp experiments and the evolved gases were analyzed afterwards.

Experimental

Electrode preparation

Double-sided graphitic and micro-crystalline Si-based negative electrodes were kindly provided by LG ES. Graphitic electrodes exhibited an areal capacity of 5.5 mAh cm^{-2} per electrode side, whereas Si-based electrodes had an areal capacity of 8.5 mAh cm^{-2} per electrode side.

One-sided positive electrodes based on $LiNi_{0.6}Mn_{0.2}Co_{0.2}O_2$ (NMC622) as the active material were produced by an in-house pilot battery line. The NMC622-based electrodes were composed of 95 wt% active material (NMC622, BASF), 2 wt% carbon black (Super C65, Imerys Graphite & Carbon) as a conductive additive and 3 wt% polyvinylidene difluoride (PVdF) as a binder (Solef 5130, Syensqo). The average areal capacity of these electrodes was 5.2 mAh cm^{-2} based on an average total electrode mass loading of 31.3 mg cm^{-2} at a practical capacity of 175 mAh g^{-1}. All electrodes were dried under reduced pressure at 120 °C prior to cell assembly.

Cell assembly

Coin cells were assembled in a CR2032 configuration with graphitic and Si-based electrodes, respectively, as negative electrodes (15 mm diameter) and NMC622-based positive electrodes (14 mm diameter). The electrodes were separated by a monolayer polyolefin separator (Celgard 2500, 16 mm diameter). The separator was soaked with 50 μL of electrolyte consisting of 1 M $LiPF_6$ in ethylene carbonate (EC) and ethyl methyl carbonate (EMC, E-Lyte Innovations GmbH) (EC : EMC = 3 : 7 wt) with 2 wt% of vinylene carbonate (VC, Targray). Pouch cells were assembled with the same components (separator, positive and negative electrodes, electrolyte) as the abovementioned coin cells. Separators and electrodes were cut with a manual toggle press (mäder pressen GmbH, L-EP 750-40) using customized punches (mäder pressen GmbH). The coated area of the negative electrodes had a size of 121 mm × 68 mm, the coated area of the positive electrodes had dimensions of 119 mm × 66 mm and the separators exhibited dimensions of 124 mm × 71 mm. For two-layered pouch cells, two one-sided positive electrodes and one double-sided negative electrode were stacked with one separator layer in between. Accordingly, four one-sided positive electrodes and two double-sided negative electrodes were stacked with a total of four separator layers to obtain four-layered pouch cells. Therein, the uncoated aluminum sides of the inner positive electrodes faced each other so that every coated anode side faced a coated cathode side. Two-layered and four-layered pouch cells exhibited total theoretical capacities of 800 mAh and 1600 mAh, respectively, with N/P ratios of 1.11 for graphite-based cells and 1.71 for Si-based cells. Copper current collectors of the negative electrodes were connected with nickel tabs and aluminum current collectors of the positive electrodes were connected with aluminum tabs, each by ultrasonic welding (Branson, Ultraweld L20). After electrolyte addition, the electrode stacks were sealed in pouch foil under reduced pressure (Audion, Audionvac). The amount of electrolyte was calculated by multiplying the pore volume of separators and electrodes with a factor of 1.6, resulting in electrolyte volumes of 2.06 mL for four-layered pouch cells with graphitic negative electrodes and 1.51 mL for two-layered pouch cells with Si-based negative electrodes. Accordingly, the resulting volumes were 4.12 mL and 3.02 mL, respectively, for the four-layered cells. All cells were assembled at 20 °C under a dry room atmosphere with a dew point below −60 °C.

Electrochemical investigations

Electrochemical charge/discharge cycling was conducted using a Maccor 4000 battery tester at 20 °C. After a wetting step of at least 10 h, two charge/discharge cycles were applied to each cell as a formation procedure. These consisted of constant current (CC) charging steps with 0.02C and CC discharging steps with 0.05C within cutoff voltages of 4.3 V and 3.0 V for graphitic cells, and 4.3 V and 2.5 V for Si-based cells. After this formation procedure, a CC charging step with 0.02C to 4.3 V was applied. All charging steps were terminated by a constant voltage step when a current <0.01C was reached. Herein, a C-rate of 1C equals 5.2 mA cm^{-2} corresponding to the areal capacity of the positive electrode. For pouch cells, pressure plates were applied to improve the contact between the electrodes.

Cell disassembly

For thermal analysis at the combinations level, coin cells and pouch cells were disassembled in an argon-filled glovebox (O_2 and H_2O < 0.1 ppm, MBraun). For coin cells, a custom-made disassembly tool was used and the cells were separated into their individual components. Pouch cells were opened using ceramic scissors and also separated into their individual components.

Differential scanning calorimetry

Differential scanning calorimetry (DSC) was conducted using a Q2000 calorimeter (TA Instruments). Negative electrodes were punched into 4 mm discs and two of these discs were encapsulated in high-pressure stainless-steel pans (TA Instruments) together with 7.5 μL of electrolyte each (the same amount was used for the pure electrolyte baseline measurement). DSC measurements were performed under a nitrogen flow rate of 50 mL min^{-1}. After equilibration at 20 °C for two minutes, the samples were heated to 400 °C at a heating rate of 5 °C min^{-1}. All experiments were conducted three times.

Heat ramp experiments

Thermal analysis of pure electrolyte and of the combination of charged negative electrodes with the electrolyte was performed in closed titanium vessels (THT, 8 mL volume) in an ARC (ARC 254, Netzsch). For the investigation of negative electrodes, one-third (27 cm^2) of a complete double-sided electrode was cut into small pieces and put into a titanium vessel. One-third of the electrolyte amount of a two-layered pouch cell was added to simulate the reactions within the cells with comparable electrode/electrolyte ratios. This resulted in a volume of 688 µL of fresh electrolyte for the graphitic electrodes and 502 µL of fresh electrolyte for the Si-based electrodes. For the investigation of pure electrolyte, 502 µL of electrolyte was added to the titanium vessel. The vessel was connected to the ARC device under argon counterflow. A heat ramp with a constant heating rate of 1 °C min^{-1} from room temperature to 300 °C was applied and the heater temperature and the sample temperature were monitored using separate thermocouples. Simultaneously, the pressure inside the vessel was monitored throughout the experiment. After subsequent cooling of the sample to room temperature, the generated gases were extracted to a Tedlar® gas sampling bag for analysis by gas chromatography (GC) with a barrier discharge ionization detector (BID) and a thermal conductivity detector (TCD). The experimental setup is schematically depicted in Fig. 1.

Gas analysis

To analyze the evolved gases, GC measurements were performed on a GC-2010 Plus system (Shimadzu Deutschland GmbH, Germany) with GC parameters and calibration adapted from Leißing *et al.*[47] For the quantification of permanent gases (H_2, CH_4, CO, C_2H_4, C_2H_6, and CO_2), a barrier discharge ionization detector (BID), BID-2010 Plus, and a thermal conductivity detector (TCD), TCD-2010 Plus (both Shimadzu Deutschland GmbH), were utilized. Chromatographic separation was performed on a PLOT gas separation column, RT®-Msieve5 A (30 m × 0.32 mm × 30 µm), for GC-BID and on a packed RT®-Shin-CarbonST (80/100, 2.0 m × 0.53 mm) column for GC-TCD measurements, both by Restek. Injections from the Tedlar® bags were done manually with 25–100 µL syringes (Hamilton Company). LabSolutions and Postrun Analysis editor (version5.90, Shimadzu) were used to control the system and evaluate the resulting chromatograms.

Heat–wait–seek accelerating rate calorimetry

Four-layer pouch cells were investigated by accelerating rate calorimetry (ARC) in an EVx Accelerating Rate Calorimeter (THT) in heat–wait–seek (HWS) mode. For each measurement, a sample thermocouple was attached concentrically at the pouch cell with aluminum adhesive tape and the cell was fixed using a stainless-steel cell holder hanging at the calorimeter lid. The experiments in HWS mode were started by heating and equilibrating the cell to 30 °C and the temperature was increased in steps of 5 °C. After a wait time of 40 min after each heating step, exothermic behavior was sought for 10 min with a sensitivity threshold of 0.02 °C min^{-1}. If a self-heating rate of $d\vartheta/dt \geq 0.02$ °C min^{-1} was detected, the system switched into exothermic mode by always equalizing the sample and calorimeter chamber temperatures to achieve quasi-adiabatic conditions. If no exothermic behavior was detected ($d\vartheta/dt < 0.02$ °C min^{-1}), the abovementioned, stepwise HWS procedure was continued. Measurements were finished after thermal runaway of a cell or when reaching 300 °C without detection of exothermic reactions leading to a self-heating rate of $d\vartheta/dt \geq 0.02$ °C min^{-1}.

Prior to HWS-ARC experiments with pouch cells, a calibration of the calorimeter and its thermocouples was conducted to exclude any temperature drift not caused by exothermic or endothermic processes in the cell. For calibration, an aluminum dummy was heated in steps of 50 °C between 50 °C and 300 °C. The temperature offset between the heater thermocouples and the sample thermocouple was recorded at each temperature, so the software could compensate for this in subsequent measurements. The accuracy of the calibration was checked in a drift test. Therein, an aluminum dummy was heated in steps of 25 °C (between 30 °C and 300 °C) and it was checked whether endothermic or exothermic behavior was detected (0.02 °C $min^{-1} < d\vartheta/dt < 0.02$ °C min^{-1}).

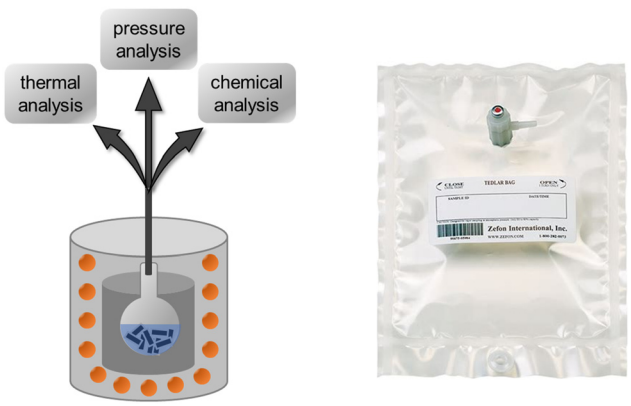

Fig. 1 Schematic setup for the heat-ramp experiments (left) and an image of a Tedlar® gas sampling bag for gas sampling (right).

Results and discussion

Thermal stability at the material/combinations level

DSC investigations of graphitic and Si-based negative electrodes were performed to directly compare the thermal stability of these negative electrode active materials. Since the electrolyte is directly involved in exothermic decomposition reactions with the electrode in an LIB, and is therefore also relevant for thermal stability, the electrodes were always investigated in combination with fresh electrolyte. To obtain a fair comparison, all electrodes were charged to the same capacity in a coin cell and two small pieces of electrode were used for every DSC measurement with a total capacity of 1.3 mAh each. Despite all investigated electrodes having the same capacity, it has to be noted that the SOC differed between the two negative active

materials due to the different areal capacities of the electrodes. This resulted in an SOC of 90% for the graphitic electrodes and an SOC of 60% for the Si-based electrodes (each referred to the theoretical specific capacity of 372 mAh g^{-1} and 3579 mAh g^{-1}, respectively). However, the capacity of Si-based electrodes is not necessarily used completely for application either since the partial utilization provides comparably high capacities and energy densities as well. Therefore, it is a fair comparison to always investigate electrodes with the same capacity. Besides the capacity, the SOC of the electrodes certainly affects the thermal stability. Its impact in the case of Si-based electrodes is currently under investigation; however, it is beyond the scope of this study. For the NMC622-based electrodes, an SOC of 100% was obtained (referred to the practical capacity of 175 mAh g^{-1}).

For the pure electrolyte, the heat flow shown in Fig. 2 exhibits a first endothermic reaction starting at 220 °C, which is followed by exothermic decomposition reactions above 250 °C. This is in good agreement with previous investigations by Botte *et al.*, who analyzed the thermal behavior of electrolytes containing $LiPF_6$, EC and EMC in different compositions.[48] The endothermic behavior can be assigned to reactions between the conducting salt $LiPF_6$ and the organic carbonate EMC. At elevated temperatures, $LiPF_6$ decomposes to LiF and the strong Lewis acid PF_5, which subsequently reacts with EMC. The occurring reactions could be very similar to the proposed reaction mechanism by Kawamura *et al.* for the electrolyte decomposition containing $LiPF_6$, EC and diethyl carbonate (DEC) since the electrolyte only differs in having DEC instead of EMC with an ethyl instead of a methyl group.[49]

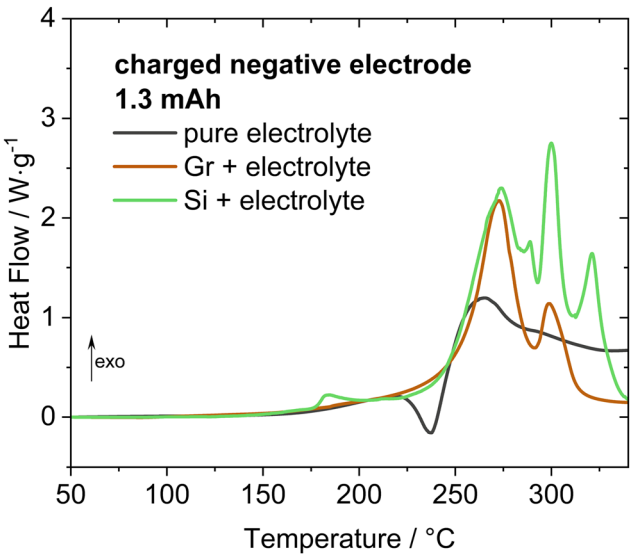

Fig. 2 DSC investigation of pure electrolyte and charged graphitic and Si-based negative electrodes, respectively, in combination with fresh electrolyte. For both materials, negative electrodes with the same capacity of 1.3 mAh were investigated. Due to the different areal capacities of the two electrodes, graphitic electrodes were analyzed at an SOC of 90%, whereas Si-based electrodes had an SOC of 60%.

For the Si-based electrode, the first exothermic decomposition reaction was observed at 180 °C, depicted as a minor increase of the heat flow in Fig. 2. It is assumed that, similar to the graphitic active material,[31] the decomposition of thermally unstable and rather organic SEI components exposes the surface of lithiated Si particles to the electrolyte and enables exothermic decomposition reactions of the electrolyte on the particle surface. It is proposed that the Si active material is also involved in these decomposition reactions, whereas for the graphitic electrodes, only the intercalated lithium reacts with the electrolyte at the electrode surface. The graphitic structure is not involved in these decomposition reactions, leading to the absence of a distinct heat flow increase at 180 °C in comparison with Si-based electrodes. Above 220 °C, the heat flow started to rise similarly for both negative electrodes until it reached a first maximum at 274 °C. As the pure electrolyte decomposed in the same temperature range, this rising heat flow observed for the combination of a charged negative electrode with electrolyte is indicated to be initiated by the electrolyte decomposition and the presence of electrolyte decomposition products is shown to be crucial for the thermal behavior of charged negative electrodes. However, additional exothermic reactions with a higher total heat generation were determined in the presence of active materials compared to the pure electrolyte. Except for the small heat flow increase at 180 °C for the Si-based electrode, the thermal behavior of both negative electrode active materials is comparable for temperatures up to 280 °C. In this temperature range, the investigated graphitic electrodes exhibited an amount of released heat of 680 J g^{-1}, while the Si-based electrodes released 720 J g^{-1} of heat. Above 280 °C, the Si-based electrodes exhibited an increased heat flow, and thus an increased reactivity in comparison with the graphitic electrodes. This is depicted by a highly increased total amount of released heat of 1700 J g^{-1} for Si-based electrodes compared to 930 J g^{-1} for graphitic ones, which indicates different decomposition mechanisms for both active materials.

In general, the onset of exothermic reactions in LIBs is ascribed to the negative electrode at temperatures of *ca.* 100 °C, with initially little generated heat. Since the DSC investigations in this study were only performed with small sample sizes in comparably heavy stainless-steel pans, the measurements exhibit low sensitivity. Thus, the first exothermic decomposition reactions could only be detected at 180 °C. However, the strongly rising heat flows for both negative electrodes at 250 °C show that the negative electrode can also contribute to the thermal runaway of a battery cell.

To conclude, thermal analysis at the single material level and material combinations level enables thermal profiling of different battery components, such as the electrolyte combined with different electrodes, as reported in the literature.[32,37,50] Yet the conducted DSC analysis is limited to thermal information and cannot reveal cross-talk reactions. For the application of LIBs, cell venting is relevant for its safety as well, which makes pressure monitoring valuable to determine the safety properties of LIB components and complete cells.

Moreover, analysis of evolving gases can enable conclusions on both reaction mechanisms and the reactivity of these evolving gases.

To enable thermal analysis combined with pressure and gas analysis, charged graphitic and Si-based electrodes in combination with fresh electrolyte were heated with a constant heat ramp in a closed vessel within an ARC and both the sample and heater temperature as well as the pressure were monitored during heating to 300 °C. Fig. 4 shows the thermal behavior of these samples and of the pure electrolyte. Without exothermic reactions, the sample temperature follows the heater temperature, resulting in a linear temperature increase. Simultaneously, the pressure inside the closed vessel rises due to the increased temperature. It has to be noted that the pressure was normalized to the mass of added electrolyte, as shown in Fig. 4b, to improve the comparability among the samples. In the case of exothermic reactions, the sample temperature and the pressure started to rise faster compared to the aforementioned behavior.

For both the graphitic and the Si-based electrodes, the sample temperature started to rise above the heater temperature at 215 °C. This temperature is higher compared to the onset temperature observed in DSC investigations since the sensitivity is lower for this method. The sample temperature of both combinations of electrode with electrolyte rapidly increased at 240 °C due to exothermic decomposition reactions of the electrode active material and the electrolyte. This abrupt temperature increase is given as the thermal runaway temperature (ϑ_{TR}) in Table 1. However, the graphitic electrodes reached a maximum temperature (ϑ_{max}) of 450 ± 10 °C, whereas the Si-based electrodes exhibited a highly increased ϑ_{max} of 720 ± 30 °C. This indicates highly exothermic reactions in the case of charged Si despite the total capacity, *i.e.*, Li content, being the same for both active materials and suggests that the complete structure of the lithiated Si particles is involved in the decomposition reactions. In contrast, only the intercalated Li exothermically reacts with the electrolyte in the case of the graphitic electrode, resulting in a distinctly lower maximum temperature. It can be concluded that not only is the amount of included Li decisive for the thermal stability and the reactivity of the electrodes at elevated temperatures but the possibly occurring exothermic decomposition mechanisms are also important for the safety properties. These decomposition mechanisms were shown to be different for graphitic and Si-based electrodes by the different thermal behaviors at the same Li content. A schematic comparison of the thermal decomposition of both active materials is illustrated in Fig. 3: (i) for lithiated graphite, exothermic reactions are initiated by the thermally induced Li deintercalation, followed by the formation of an intermediate passivation layer. Eventually, Li is completely deintercalated while the structural integrity of graphite is maintained. (ii) In comparison, Li_xSi_y reacts with the electrolyte on the complete surface, leading to a progressing degradation, finally involving the complete Li_xSi_y-structure.

For the pure electrolyte, the pressure inside the vessel slowly rose due to the increased temperature, until thermal decomposition started at a heater temperature of 200 °C resulting in a more pronounced pressure increase. At 230 °C, the pressure increase slowed down again, until a maximum pressure of 40 ± 1 bar $g^{-1}_{electrolyte}$ was reached at the termination temperature of 300 °C. When the sample cooled down to 30 °C, the pressure decreased and the pressure difference $\Delta p_{30\ °C}$ before and after the measurement at 30 °C was used as an indicator for the amount of generated gases.

In contrast to the highly different maximum temperatures at similar onset temperatures, both negative electrode materials showed comparable pressure buildup evolution behavior. The pressure rapidly increased to 55 ± 4 bar $g^{-1}_{electrolyte}$ for graphite and 56 ± 3 bar $g^{-1}_{electrolyte}$ for Si, when the fast temperature rise was also observed. Here, the pressure increase was delayed compared to the pure electrolyte as the generated

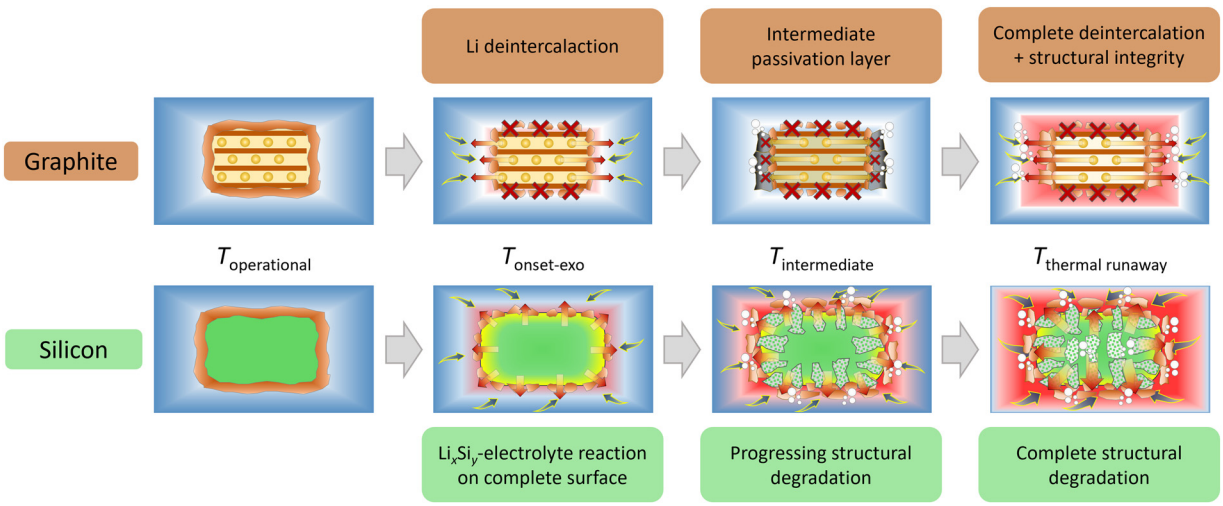

Fig. 3 Schematic illustration comparing the structural decomposition of graphitic and Si-based negative electrodes with increasing temperature.

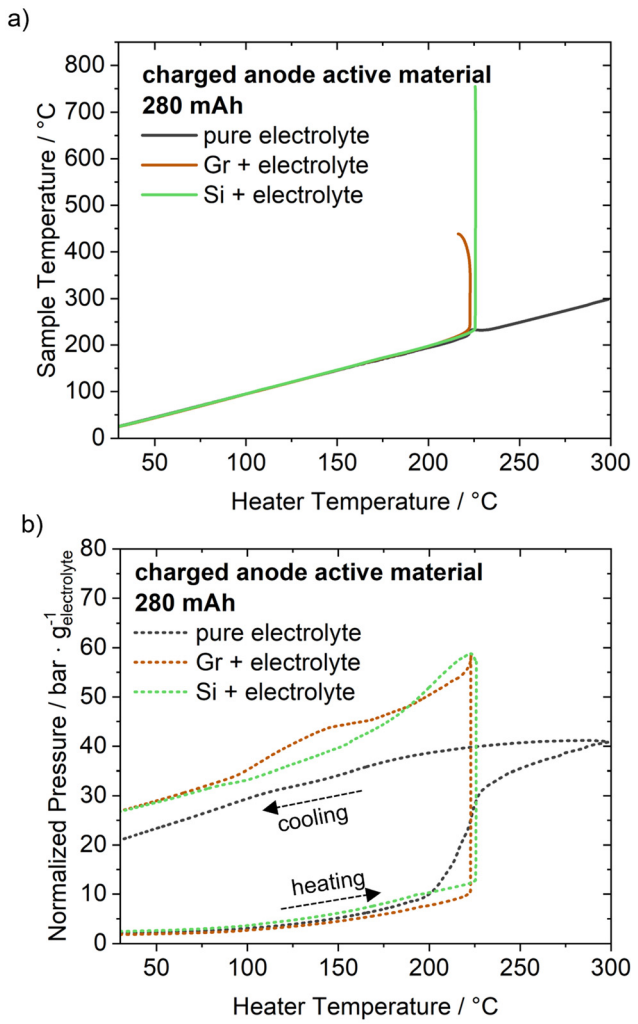

Fig. 4 Heat-ramp experiments of pure electrolyte and of the combination of charged graphitic and charged Si-based electrodes with fresh electrolyte with (a) the sample temperature and (b) the normalized pressure plotted against the heater temperature. Since the amount of added electrolyte was adjusted to the amount of electrolyte in a complete cell (corresponding to pore volume of separator and both electrodes), the pressure was normalized to the mass of the added electrolyte for improved comparability. Here, only one measurement per experimental setup is shown. The set with two measurements each can be found in Fig. S1.

Table 1 Summary of characteristic parameters from heat-ramp experiments

Sample	ϑ_{TR}/°C	ϑ_{max}/°C	p_{max}/ bar $g^{-1}_{electrolyte}$	$\Delta p_{30\ °C}$/ bar $g^{-1}_{electrolyte}$
Pure electrolyte	—	300[a]	40.3 ± 0.9	18.4 ± 0.4
Gr + electrolyte	240 ± 1	450 ± 10	55 ± 4	24.4 ± 0.6
Si + electrolyte	238 ± 2	720 ± 30	56 ± 3	23 ± 1

[a] The maximum temperature of 300 °C for the pure electrolyte was reached as the termination criterion for the measurement.

gases of the electrolyte decomposition were initially consumed at the electrode surfaces. After cooling down to 30 °C, a slightly increased pressure was obtained in comparison with the pure electrolyte (see Table 1), which marks increased gas generation for the combination of the active material with the electrolyte. Although the Si-based electrodes exhibited more exothermic decomposition dynamics than the graphitic electrodes, this did not lead to a higher amount of generated gases, as can be seen by the similar pressure buildups. To conclude, the combination of graphitic and Si-based electrodes with the electrolyte exhibited highly exothermic decomposition reactions at similar onset temperatures and also similar pressure evolutions. However, both negative electrodes distinctly differed in the maximum temperature, indicating a higher reactivity for Si-based electrodes.

The gas compositions of the heated samples of the pure electrolyte as well as of the combinations of both negative electrodes with electrolyte after the cool down step are shown in Fig. 5. The pure electrolyte exhibited typical gaseous products in terms of EC/EMC decomposition with carbon dioxide as the main gas species[51–53] and ethylene as the major component for the decomposition of EMC.[54] In addition, a high amount of 35% of gases was not identified as one of the six detected gases for the pure electrolyte decomposition. Reasonable decomposition products for the utilized electrolyte include hydrocarbons larger than the ones identified here, such as propane, as well as fluorinated hydrocarbons and fluorophosphates.[51,52] For the graphitic electrodes, the relative gas amounts of carbon dioxide and ethylene decreased to 9% and 6%, respectively, as the pure electrolyte decomposition was reduced and decomposition reactions with the intercalated lithium occurred instead. In addition, ethane was also generated (8%), which could partly originate from subsequent reactions of ethylene as an

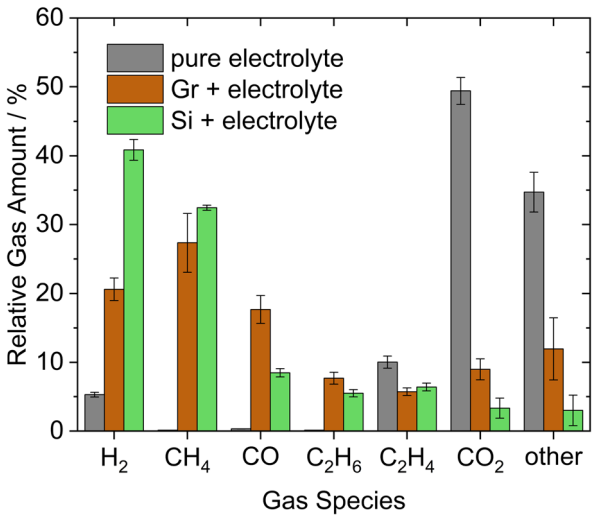

Fig. 5 Gas composition of pure electrolyte and of the combination of charged graphitic and charged Si-based electrodes with fresh electrolyte after heating to 300 °C and subsequent cooling to 30 °C. The relative gas amount is given by volume.

intermediate from the pure electrolyte decomposition. But in particular, the relative gas amounts of toxic carbon monoxide (18%) and the combustible gases methane (27%) and hydrogen (21%) increased in comparison with the pure electrolyte (pure electrolyte: 0.3% CO, 0.1% CH_4 and 5% H_2). These gases were shown to be the products of various decomposition reactions of lithiated graphite with electrolyte and binder.[55,56] For the charged Si-based electrodes, the relative gas amounts of the three detectable hydrocarbons methane, ethane and ethylene were comparable to the amounts of the graphitic electrodes. However, the relative amounts of carbon monoxide and carbon dioxide were distinctly reduced for charged Si, which could be explained by the predominant formation of lithium silicates and the consumption of oxygen-containing species from the organic carbonates in the case of Si-based electrodes. Simultaneously, the generation of hydrogen was strongly increased, making hydrogen the gas species with the highest relative gas amount at 41%. Therein, the rising hydrogen evolution from pure electrolyte to graphitic electrodes and finally to Si-based electrodes is particularly remarkable. For the pure electrolyte, the generation of hydrogen was comparatively low, which was also reported for the thermal decomposition of different organic carbonates in combination with $LiPF_6$,[52] whereas the addition of charged graphite to the electrolyte induced a distinct increase in hydrogen evolution. SEI components such as lithium ethylene glycol could contribute to hydrogen evolution in the presence of HF and deintercalated lithium under thermal abuse.[57] In particular, the presence of reactive lithium is considered the origin of the increased hydrogen evolution. The participation of Si in the thermal decomposition reactions led to elevated hydrogen evolution compared to graphitic electrodes. Therein, silanol surface groups could react with HF and other electrolyte decomposition products, as also described by Seitzinger *et al.*,[58] to form Si oxides and hydroxides as intermediates that eventually decompose and contribute to hydrogen evolution. Consequently, the continuous progression of the thermal decomposition through the complete lithiated Si particle structure resulted in the generation of a highly elevated amount of hydrogen. As hydrogen is highly reactive, its generation illustrates a critical safety risk regarding subsequent exothermic reactions in a complete battery cell. For instance, the evolution of oxygen from charged, *i.e.*, delithiated, NMC-based positive electrodes at elevated temperatures[35] could lead to severe exothermic oxyhydrogen reactions. The reaction mechanism which is responsible for hydrogen generation of charged Si-based electrodes needs to be resolved and is a major focus of current studies.

In conclusion, gas analysis revealed decreasing amounts of non-reactive carbon dioxide and simultaneously increasing amounts of combustible gases – especially hydrogen – from the pure electrolyte to the graphitic electrodes and finally to the Si-based electrodes. This is concomitant with reduced safety properties for Si-based electrodes in comparison with graphitic electrodes and marks a relevant addition to DSC investigations, which exhibited comparable thermal properties for both negative electrodes.

Thermal stability at the cell level

To determine the impact of graphitic and Si-based negative electrodes not only at the combinations level but also at the battery cell level, four-layer pouch cells with NMC622-based positive electrodes were assembled and investigated in the charged state by ARC in HWS mode. To enable direct comparability of both negative electrode active materials, the same NMC622-based positive electrodes were used, ensuring the same total capacity for all investigated pouch cells. Thus, all NMC622-based electrodes exhibited an equal degree of delithiation and the negative electrodes contained an equal Li amount.

By using HWS-ARC, the thermal behavior of complete battery cells can be investigated, as shown by the temperature progression and the self-heating rates shown in Fig. 6. For both cells containing graphitic and Si-based negative electrodes, the first exothermic reactions were detected at similar onset temperatures (115 ± 2 °C for graphitic cells *vs.* 113 ± 8 °C for Si-based cells). After the onset of exothermic reactions, the temperature increased much faster for the Si-based cells, which led to a six times shorter duration between the onset of exothermic reactions and thermal runaway of the cell. Herein, the thermal runaway was identified as a sudden increase of the self-heating rate. This period of time was determined to be 87 ± 9 min for the Si-based cells, whereas it lasted 500 ± 100 min for the graphitic cells to enter thermal runaway after the onset of exothermic reactions due to a much slower temperature increase.

The accelerated reactivity of Si-based cells was confirmed by increased self-heating rates in comparison with graphitic cells, as shown in Fig. 6c. The cells with graphitic negative electrodes showed low self-heating rates at the onset temperature and the self-heating rates steadily increased with rising temperatures. In contrast, the temperature of the Si-based cells increased comparably rapidly with self-heating rates of up to 10 °C min^{-1} immediately at the onset of exothermic reactions, which implies different kinetics for the thermal decomposition of graphitic and Si-based electrodes, respectively. It can be assumed that the increased volumetric capacity of Si compared to graphite (2190 mAh cm^{-3} for Si *vs.* 735 mAh cm^{-3} for graphite), and thus the elevated lithium concentration at the Si particle surface, led to an increased heat generation at the onset of exothermic reactions. The initially high self-heating rate is particularly remarkable since a self-heating rate of 10 °C min^{-1} is regularly used as a threshold to define the thermal runaway of a battery cell in the literature.[37,59] However, the Si-based cells had not yet entered thermal runaway at this temperature, but the self-heating rate decreased afterwards as a new protective layer of decomposition products was generated and decelerated the exothermic reactions, until the self-heating rate rose again above 130 °C up to the thermal runaway. This difference in the development of self-heating rates for the investigated cells indicates different reaction mechanisms for the thermal behavior of graphitic and Si-based negative electrodes, as the negative electrode active material showed the only difference for the investigated cells. The determined

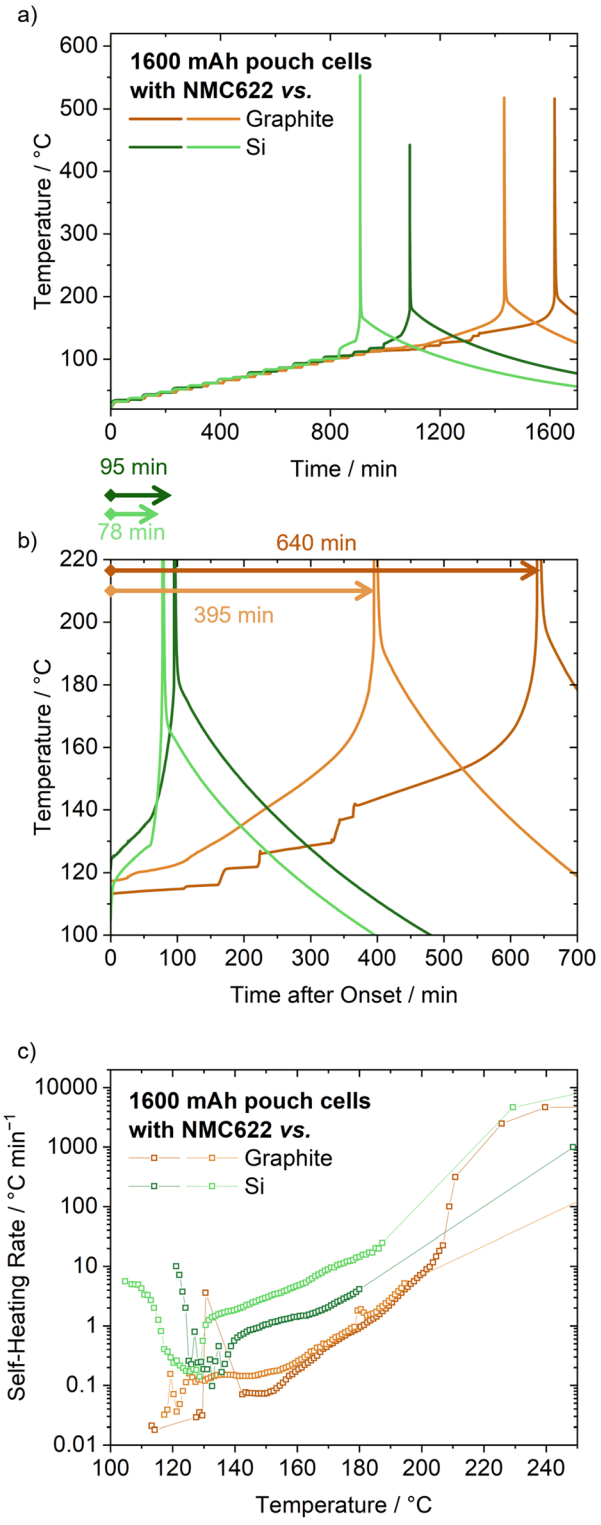

Fig. 6 HWS-ARC investigations of four-layer pouch cells with graphitic and Si-based negative electrodes. (a) The temperature for the complete measurements until thermal runaway of the cells. (b) A magnified extract with the onset of exothermic reactions as the starting point on the *x*-axis and times given from the onset until thermal runaway. (c) Self-heating rates for the complete measurements until thermal runaway.

differences could be attributed to the different structures of the two active materials in the charged and lithiated state with Li intercalation for graphite and Li insertion for Si, as also illustrated in Fig. 3. With increasing temperature, intercalated Li from the graphitic structure is thermally deintercalated and exothermically reacts with the electrolyte since the SEI as a protective layer simultaneously partly decomposes.[31] This leads to continuous heat generation and typically to a continuously increasing self-heating rate for graphitic cells between the onset of exothermic reactions and thermal runaway.[31,59] For Si-based cells, the complete structure of lithiated Si was indicated to be involved in decomposition reactions with the electrolyte, leading to comparably high self-heating rates immediately at the onset of exothermic reactions. After a short decline of the self-heating rates, this decomposition of the complete Si structure also resulted in distinctly increased self-heating rates compared to graphitic cells (note the logarithmic scale in Fig. 6c). In addition, the Si-based cells entered thermal runaway at lower temperatures than graphitic cells (184 ± 4 °C for Si *vs.* 201 ± 6 °C for graphite). This matches the gas analysis data, shown in Fig. 5, since the increased generation of combustible gases for Si-based electrodes leads to an increased reactivity at the cell level, when oxygen is released at the positive electrode due to phase transitions of the NMC active material.

These phase transitions with concomitant oxygen release are often considered a driver of thermal runaway in LIBs.[35,60] This is also indicated for the investigated cells with graphitic negative electrodes since thermal runaway of these cells was observed at 201 ± 6 °C and oxygen release of NMC622-based electrodes with a comparable specific capacity (175 mAh g^{-1} at 4.3 V) was reported to occur in close proximity to 200 °C.[32,35,61] Replacing NMC622 as a cathode active material with $LiFePO_4$ would therefore improve the cell's thermal stability by shifting thermal runaway to higher temperatures or even preventing thermal runaway completely.[37,62,63] In contrast, the thermal runaway of the investigated cells with Si-based electrodes already occurred below 200 °C, thus, prior to oxygen release from the NMC active material. Therefore, it was concluded that the thermal runaway was initiated by the negative electrode in Si-based cells. This characteristic of Si-based electrodes being the initiator of both the onset of exothermic reactions and the thermal runaway shows a similarity to Li metal electrodes that were reported to be capable of initiating thermal runaway.[40] Since graphitic electrodes are typically only responsible for the onset of exothermic reactions, different decomposition kinetics is indicated for graphite and Si with the involvement of the complete structure of the lithiated Si particles in the decomposition reactions.

In conclusion, the Si-based cells exhibited distinctly worse thermal safety properties in comparison with graphitic cells with the same NMC622-based positive electrodes and the same total capacity. This was depicted by a faster occurrence of a thermal runaway at lower temperatures for Si-based cells, which shortens the time to potentially take measures to prevent thermal runaway of a cell in application.

Conclusions

In this study, the thermal behavior of graphitic and Si-based negative electrodes was compared at the combinations level with electrolyte up to the cell level to assess the thermal safety properties of LIBs with these electrodes. At the combinations level with comparably small amounts of active material, DSC investigations indicated decreased thermal stability for the combinations of charged electrodes with electrolyte compared to pure electrolyte, but a similar thermal stability among both active materials. However, it was shown that DSC investigations are not sufficient to determine all safety-relevant thermal properties as the combination of thermal analysis with pressure and gas analysis provided additional insights into the thermal behavior of the electrodes. Exothermic reactions of charged Si-based electrodes with electrolyte caused considerably higher temperatures than reactions of charged graphitic electrodes with the same total capacity and the same electrolyte composition, while the thermal decomposition of the pure electrolyte led to lesser heat and gas generation. Moreover, the gas composition of the generated gases of the combination of both active materials with electrolyte differed. The amounts of carbon dioxide and toxic carbon monoxide were reduced for Si-based electrodes compared to graphitic electrodes, whereas the increased amounts of methane and especially hydrogen as combustible gases are remarkable and safety-relevant for LIBs. These gases can initiate severe exothermic reactions in a battery cell, such as oxyhydrogen reactions with oxygen, released from charged cathode active material at elevated temperatures.

These observations at the material combinations level were confirmed by HWS-ARC investigations at the cell level. It was shown that cells with Si-based negative electrodes exhibited a similar onset temperature for exothermic reactions compared to cells with graphitic negative electrodes, but directly started with distinctly higher self-heating rates at the onset temperature. In contrast to continuously rising self-heating rates for the graphitic cells, the self-heating rates of the Si-based cells decreased after the onset temperature and increased afterwards until thermal runaway, indicating different decomposition mechanisms for both active materials. Due to higher self-heating rates for the Si-based cells, these cells entered thermal runaway distinctly faster than graphitic cells.

In summary, this study revealed major differences in the thermal stability of graphitic and Si-based negative electrodes, which are safety-relevant properties for application in LIBs. Based on these findings, strategies can be developed to deal with the decreased thermal stability of Si-based electrodes. Limited utilization of the comparably high specific capacity of Si could improve the thermal stability by decreasing the reactivity of Si-based electrodes at lower SOCs. Moreover, the optimization of the electrolyte composition could help improve the thermal stability of the SEI, and thus the onset temperature of exothermic reactions, while also reducing the amount and the hazardousness of generated gases.

Finally, as the reactivity of the anode with the electrolyte strongly depends on what type of anode surface is in direct contact with the electrolyte, reactive/less reactive composite electrode matrix concepts, where the reactive material (in this case, Si) is embedded into a less reactive material (in this case carbon), will be further explored to avoid direct contact of Si with the electrolyte.

The investigation of critical factors for the thermal behavior of Si-based electrodes and the identification of thermal decomposition mechanisms for these electrodes are the focus of current studies.

Author contributions

Lukas Schrief: conceptualization, investigation, writing – original draft, methodology, and visualization. Lukas Trojahn: investigation and methodology. Junyeong Jang: investigation. Nick Fehlings: investigation. Sascha Nowak: supervision and writing – review & editing. Martin Winter: supervision and writing – review & editing. Markus Börner: writing – review & editing, supervision, and project administration.

Conflicts of interest

The authors declare no conflicts of interest.

Data availability

The data supporting this article have been included as part of the supplementary information (SI). Supplementary information is available. See DOI: https://doi.org/10.1039/d6eb00051g.

Acknowledgements

The authors acknowledge LG Energy Solution for funding within the Frontier Research Laboratory (FRL) program.

References

1 T. Placke, R. Kloepsch, S. Dühnen and M. Winter, *J. Solid State Electrochem.*, 2017, **21**, 1939–1964.
2 G. Zubi, R. Dufo-López, M. Carvalho and G. Pasaoglu, *Renewable Sustainable Energy Rev.*, 2018, **89**, 292–308.
3 M. S. Guney and Y. Tepe, *Renewable Sustainable Energy Rev.*, 2017, **75**, 1187–1197.
4 Y. Tang, Y. Zhang, W. Li, B. Ma and X. Chen, *Chem. Soc. Rev.*, 2015, **44**, 5926–5940.
5 M. N. Obrovac and V. L. Chevrier, *Chem. Rev.*, 2014, **114**, 11444–11502.
6 R. Schmuch, R. Wagner, G. Hörpel, T. Placke and M. Winter, *Nat. Energy*, 2018, **3**, 267–278.
7 M. N. Obrovac and L. J. Krause, *J. Electrochem. Soc.*, 2007, **154**, A103.

8 I. Dienwiebel, M. Winter and M. Börner, *J. Phys. Chem. C*, 2022, **126**, 11016–11025.
9 K. Feng, M. Li, W. Liu, A. G. Kashkooli, X. Xiao, M. Cai and Z. Chen, *Small*, 2018, **14**, 1702737.
10 A. Franco Gonzalez, N.-H. Yang and R.-S. Liu, *J. Phys. Chem. C*, 2017, **121**, 27775–27787.
11 X. Su, Q. Wu, J. Li, X. Xiao, A. Lott, W. Lu, B. W. Sheldon and J. Wu, *Adv. Energy Mater.*, 2014, **4**, 1300882.
12 C. K. Chan, H. Peng, G. Liu, K. McIlwrath, X. F. Zhang, R. A. Huggins and Y. Cui, *Nat. Nanotechnol.*, 2008, **3**, 31–35.
13 X. H. Liu and J. Y. Huang, *Energy Environ. Sci.*, 2011, **4**, 3844.
14 D. Wang, M. Gao, H. Pan, J. Wang and Y. Liu, *J. Power Sources*, 2014, **256**, 190–199.
15 L. Pan, H. Wang, D. Gao, S. Chen, L. Tan and L. Li, *Chem. Commun.*, 2014, **50**, 5878–5880.
16 Y. Yao, M. T. McDowell, I. Ryu, H. Wu, N. Liu, L. Hu, W. D. Nix and Y. Cui, *Nano Lett.*, 2011, **11**, 2949–2954.
17 J. S. Kim, W. Pfleging, R. Kohler, H. J. Seifert, T. Y. Kim, D. Byun, H.-G. Jung, W. Choi and J. K. Lee, *J. Power Sources*, 2015, **279**, 13–20.
18 Z. Cao, X. Zheng, Q. Qu, Y. Huang and H. Zheng, *Adv. Mater.*, 2021, **33**, e2103178.
19 N.-S. Choi, K. H. Yew, K. Y. Lee, M. Sung, H. Kim and S.-S. Kim, *J. Power Sources*, 2006, **161**, 1254–1259.
20 C. Xu, F. Lindgren, B. Philippe, M. Gorgoi, F. Björefors, K. Edström and T. Gustafsson, *Chem. Mater.*, 2015, **27**, 2591–2599.
21 M. Graf, C. Berg, R. Bernhard, S. Haufe, J. Pfeiffer and H. A. Gasteiger, *J. Electrochem. Soc.*, 2022, **169**, 20536.
22 Y. Cheng, Z. Guo, C. Zheng, L. Zhang, S. Wang and H. Du, *Energy Mater. Devices*, 2025, **3**, 9370055.
23 C. Essl, A. W. Golubkov, E. Gasser, M. Nachtnebel, A. Zankel, E. Ewert and A. Fuchs, *Batteries*, 2020, **6**, 30.
24 X. Feng, M. Ouyang, X. Liu, L. Lu, Y. Xia and X. He, *Energy Storage Mater.*, 2018, **10**, 246–267.
25 Z. Liao, S. Zhang, K. Li, G. Zhang and T. G. Habetler, *J. Power Sources*, 2019, **436**, 226879.
26 L. Hellweg, T. Beuse, M. Winter and M. Börner, *J. Electrochem. Soc.*, 2023, **170**, 40530.
27 R. Spotnitz and J. Franklin, *J. Power Sources*, 2003, **113**, 81–100.
28 M. N. Richard and J. R. Dahn, *J. Electrochem. Soc.*, 1999, **146**, 2068–2077.
29 H. Maleki, G. Deng, A. Anani and J. Howard, *J. Electrochem. Soc.*, 1999, **146**, 3224–3229.
30 Z. Chen, Y. Qin, Y. Ren, W. Lu, C. Orendorff, E. P. Roth and K. Amine, *Energy Environ. Sci.*, 2011, **4**, 4023.
31 M. Börner, A. Friesen, M. Grützke, Y. P. Stenzel, G. Brunklaus, J. Haetge, S. Nowak, F. M. Schappacher and M. Winter, *J. Power Sources*, 2017, **342**, 382–392.
32 Y. P. Stenzel, M. Börner, Y. Preibisch, M. Winter and S. Nowak, *J. Power Sources*, 2019, **433**, 226709.
33 A. M. Andersson, M. Herstedt, A. G. Bishop and K. Edström, *Electrochim. Acta*, 2002, **47**, 1885–1898.
34 M. Herstedt, H. Rensmo, H. Siegbahn and K. Edström, *Electrochim. Acta*, 2004, **49**, 2351–2359.
35 S.-M. Bak, E. Hu, Y. Zhou, X. Yu, S. D. Senanayake, S.-J. Cho, K.-B. Kim, K. Y. Chung, X.-Q. Yang and K.-W. Nam, *ACS Appl. Mater. Interfaces*, 2014, **6**, 22594–22601.
36 S.-M. Bak, K.-W. Nam, W. Chang, X. Yu, E. Hu, S. Hwang, E. A. Stach, K.-B. Kim, K. Y. Chung and X.-Q. Yang, *Chem. Mater.*, 2013, **25**, 337–351.
37 D. H. Doughty and E. P. Roth, *Electrochem. Soc. Interface*, 2012, **21**, 37–44.
38 F.-N. Jiang, S.-J. Yang, X.-B. Cheng, P. Shi, J.-F. Ding, X. Chen, H. Yuan, L. Liu, J.-Q. Huang and Q. Zhang, *J. Energy Chem.*, 2022, **72**, 158–165.
39 X. Feng, S. Zheng, D. Ren, X. He, L. Wang, X. Liu, M. Li and M. Ouyang, *Energy Procedia*, 2019, **158**, 4684–4689.
40 J. Neumann, L. Hellweg, M. Bela, T. Hering, M. Stan, M. Winter, S. Nowak and M. Börner, *Cell Rep. Phys. Sci.*, 2025, **6**, 102354.
41 X. Feng, D. Ren, X. He and M. Ouyang, *Joule*, 2020, **4**, 743–770.
42 S. Ohneseit, P. Finster, C. Floras, N. Lubenau, N. Uhlmann, H. J. Seifert and C. Ziebert, *Batteries*, 2023, **9**, 237.
43 I. A. Profatilova, T. Langer, J. P. Badillo, A. Schmitz, H. Orthner, H. Wiggers, S. Passerini and M. Winter, *J. Electrochem. Soc.*, 2012, **159**, A657–A663.
44 Y.-S. Park and S.-M. Lee, *Bull. Korean Chem. Soc.*, 2011, **32**, 145–148.
45 Y. Wang and J. Dahn, *Electrochem. Solid-State Lett.*, 2006, **9**, A340.
46 J.-Y. Sun, Z.-Y. Wang, X. Shen, Y. Wu and X.-B. Cheng, *Adv. Energy Mater.*, 2025, **16**, e05793.
47 M. Leißing, M. Winter, S. Wiemers-Meyer and S. Nowak, *J. Chromatogr. A*, 2020, **1622**, 461122.
48 G. G. Botte, R. E. White and Z. Zhang, *J. Power Sources*, 2001, **97–98**, 570–575.
49 T. Kawamura, A. Kimura, M. Egashira, S. Okada and J.-I. Yamaki, *J. Power Sources*, 2002, **104**, 260–264.
50 D. Ren, X. Liu, X. Feng, L. Lu, M. Ouyang, J. Li and X. He, *Appl. Energy*, 2018, **228**, 633–644.
51 C. L. Campion, W. Li and B. L. Lucht, *J. Electrochem. Soc.*, 2005, **152**, A2327.
52 J. Lamb, C. J. Orendorff, E. P. Roth and J. Langendorf, *J. Electrochem. Soc.*, 2015, **162**, A2131–A2135.
53 Q.-S. Wang, J.-H. Sun, G.-Q. Chu, X.-L. Yao and C.-H. Chen, *J. Therm. Anal. Calorim.*, 2007, **89**, 245–250.
54 Q. Wang, J. Sun and C. Chen, *Rare Met.*, 2006, **25**, 94–99.
55 X. Liu, L. Yin, D. Ren, L. Wang, Y. Ren, W. Xu, S. Lapidus, H. Wang, X. He, Z. Chen, G.-L. Xu, M. Ouyang and K. Amine, *Nat. Commun.*, 2021, **12**, 4235.
56 Y. Zheng, Z. Shi, D. Ren, J. Chen, X. Liu, X. Feng, L. Wang, X. Han, L. Lu, X. He and M. Ouyang, *J. Energy Chem.*, 2022, **69**, 593–600.
57 L. Schmidt, K. Hankins, L. Bläubaum, M. Gerasimov and U. Krewer, *Chem. Sci.*, 2025, **16**, 5118–5128.

58 C. L. Seitzinger, R. L. Sacci, J. E. Coyle, C. A. Apblett, K. A. Hays, R. R. Armstrong, A. M. Rogers, B. L. Armstrong, T. H. Bennet, N. R. Neale and G. M. Veith, *Chem. Mater.*, 2020, **32**, 3199–3210.
59 W. Zhao, M. Rohde, I. U. Mohsin, C. Ziebert, Y. Du and H. J. Seifert, *Batteries*, 2022, **8**, 15.
60 Y. Li, X. Liu, L. Wang, X. Feng, D. Ren, Y. Wu, G. Xu, L. Lu, J. Hou, W. Zhang, Y. Wang, W. Xu, Y. Ren, Z. Wang, J. Huang, X. Meng, X. Han, H. Wang, X. He, Z. Chen, K. Amine and M. Ouyang, *Nano Energy*, 2021, **85**, 105878.
61 S.-M. Bak, M. Song, Z. Shadike, A. Hunt, I. Waluyo, J. T. Sadowski, H. Yan, Y. S. Chu, X.-Q. Yang, X. Huang and Y. Shin, *Nano Energy*, 2024, **126**, 109644.
62 N. Mao, S. Gadkari, Z. Wang, T. Zhang, J. Bai and Q. Cai, *Energy*, 2023, **278**, 128027.
63 Y. Yuan, Q. Ma, X. Zhang, F. Zhang, X. Song, H. Xin, G. Zhu and H. Zhang, *Front. Chem.*, 2024, **12**, 1324840.